

IAC-14-B5.1.10

DISSECT – DEVELOPMENT OF A SMALL SATELLITE FOR CLIMATE RESEARCH

Michael Deiml

University of Wuppertal, Germany, deiml@uni-wuppertal.de

Martin Kaufmann

Research Centre Juelich, Germany, m.kaufmann@fz-juelich.de

Peter Knieling

University of Wuppertal, Germany, knieling@uni-wuppertal.de

Friedhelm Olschewski

University of Wuppertal, Germany, olsch@uni-wuppertal.de

Panagiotis Toumpas

University of Wuppertal, Germany, toumpas@uni-wuppertal.de

Martin Langer

Technical University of Munich, Germany, martin.langer@tum.de

Manfred Ern

Research Centre Juelich, Germany, m.ern@fz-juelich.de

Ralf Koppmann

University of Wuppertal, Germany, koppmann@uni-wuppertal.de

Martin Riese

Research Centre Juelich, Germany, m.riese@fz-juelich.de

The University of Wuppertal and the Research Centre Juelich are developing a small satellite for climate research (Development Initiative for Small Satellites Exploring Climate Processes by Tomography, DISSECT). This paper focuses on its mission and its science payload. Based on the three unit CubeSat form factor, the payload consists of a small spectrometer for the observation of airglow, namely O₂ atmospheric band emissions at 762 nm. These data will be used to derive temperature distribution and dynamical wave structures at the same time.

Coupling processes initiated by waves in the middle atmosphere have increasing importance for the modeling of the climate system and represent one of the larger uncertainties in this field. To support new modeling efforts spatially resolved measurements of the wave fields are needed.

In this paper, two spectrometer designs for the observation of O₂ atmospheric band emissions are discussed. These are a Spatial Heterodyne Spectrometer (SHS) and a Fabry-Perot Interferometer (FPI). Both the SHS and the FPI can be highly miniaturized. The SHS consists of a solid block and has no moving parts, which increases the reliability in orbit while allowing high precision measurements within a small volume. Both instruments have not yet been flown on a CubeSat and have high potential to increase the importance of small satellites for science missions. DiSSECT is intended as a pathfinder for future remote sensing CubeSat constellations.

I. INTRODUCTION

The middle atmosphere (stratosphere, mesosphere and lower thermosphere) is highly affected by anthropogenic activities and global change is clearly visible herein. Due to the increase of greenhouse gases, temperature decreases in this part of the atmosphere¹. The general circulation in the middle atmosphere is driven by waves generated in the lower atmosphere: Planetary waves

being of most relevance in the stratosphere and buoyancy or gravity waves driving the circulation in the mesosphere. The latter generate small scale fluctuations which can be observed in wind, temperature and trace gas distributions.

The middle atmosphere is an interface region. For the dynamics generated in the lower atmosphere affecting the entire middle and upper atmosphere including space

weather (bottom-up), and for the solar-terrestrial interaction affecting the middle- and lower atmosphere (top-down). The middle atmosphere, and especially the mesosphere and lower thermosphere (MLT), is strongly affected by solar variability, much more than the lower atmosphere. Disturbances of middle atmosphere dynamics are known to occasionally influence the dynamics of the lower atmosphere down to tropospheric weather systems and surface temperatures², implying that solar signatures observed in the troposphere may be amplified by corresponding signatures in the middle atmosphere³. Thorough scientific understanding of the middle atmosphere is a crucial prerequisite in terms of separating natural variability from potential anthropogenic impact.

Due to the fact that the atmosphere needs to be considered as a whole to understand atmospheric interactions, many climate models are currently extended to the mesosphere or even higher up^{4,5}. Although these models predict the general behavior of the middle atmosphere very well, in detail there can be large differences⁴. These differences can be caused by sub-scale processes such as gravity waves or wave mixing, which are not completely resolved in the models and have not been measured at the required level of detail so far.

Gravity wave amplitudes are quite small in the lower atmosphere, but their amplitude increases with altitude due to the decrease of atmospheric density. The horizontal wavelength of these waves varies from a few 10 km to a few thousand and the vertical wavelength is in the order of several hundred meters to a few 10 km. Gravity waves can be observed in wind, atmospheric temperature variations associated with the adiabatic movement of air parcels within the wave.

With the end of the Envisat mission in 2012 the number of satellite missions that allow measurements of middle atmospheric parameters has further decreased. Nearly all space-borne instruments have been measuring for more than a decade and will come to their end of lifetime within the next few years. It is conceivable that there will be a gap in the observation of this part of the atmosphere soon⁶.

In addition, none of the existing instruments performs measurements of atmospheric parameters relevant for characterizing gravity waves globally with sufficiently high spatial resolution. New measurement strategies are needed to provide experimental data to the latest generation of climate models in order to adjust their model parameters.

The Research Centre Juelich and the University of Wuppertal want to address these research topics with the development of a CubeSat for the measurement of highly resolved temperature data in the middle atmosphere.

A CubeSat is a highly standardized satellite, which was originally intended for academic education and evolved

to a platform for research. Low launch costs and a high number of launch opportunities, together with fast development cycles and a variety of commercial-off-the-shelf components are a few reasons for the popularity of CubeSats.

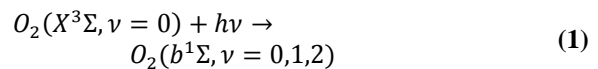
In the remaining paper, the measurement strategy of the mission and a potential technical realization is described. Two spectrometer types are compared regarding this application and the baseline concept of the whole instrument is described afterwards, followed by the CubeSat and the operational concept.

II. OXYGEN EMISSION OBSERVATION

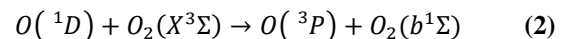
II.I. Photochemistry of Molecular Oxygen

For temperature measurements we use the emissions of $O_2(b^1\Sigma, v = 0)$ at 762 nm, the so called ‘Atmospheric Band’ (A-band). Temperature is derived from the rotational structure of this band, which follows a Boltzmann distribution. This band emission of the middle atmosphere cannot be measured from ground, because the ground state molecular oxygen in the lower atmosphere absorbs the radiation. Whereas the emission can be measured from satellites, because of the low attenuation in the thermosphere.

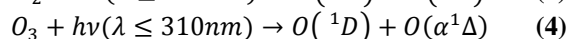
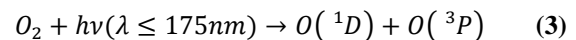
Five relevant mechanisms produce the excited oxygen state $O_2(b^1\Sigma, v = 0)$, necessary for A-band emission. Fig 1 shows the A-band volume emission rate between an altitude of 50 km and 130 km during daylight and the relevant excitation processes, as described in the following. The first two mechanisms describe the production of $O_2(b^1\Sigma, v = 0)$ through A-band photons (762 nm) and of $O_2(b^1\Sigma, v = 1)$ through B-Band photons (689 nm) from the ground state $O_2(X^3\Sigma, v = 0)$ (Reaction (1)), respectively. The oxygen with vibrational state 1 is faster deactivated to vibrational state 0 than it is quenched into the ground state⁷. Thus, this production mechanism has to be fully accounted for in the A-band emission.



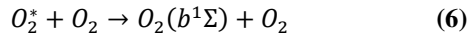
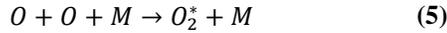
The next process is the collisional excitation of ground state oxygen by highly excited atomic oxygen $O(^1D)$, reaction (2).



The atomic oxygen state $O(^1D)$ is produced by the photolysis of molecular oxygen and ozone (Reaction (3) and (4)).



The two-step Barth process is the only excitation process, which is active during night and day. It describes the creation of oxygen O_2^* by atomic oxygen (Equation (5)), which is afterwards quenched to $O_2(b^1\Sigma)$ (Equation (6)).



This process is independent of solar radiation and can also be detected during night.

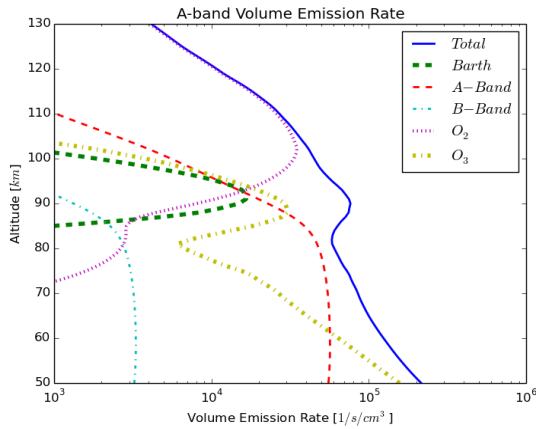


Fig 1: Contributions of different mechanisms to the total volume emission rate of the oxygen A-Band in the altitude between 50 km and 130 km.

During daytime, the O_2 A-band can be observed from the lower thermosphere down to the stratosphere, whereas during night, the radiation is limited to a small altitude range between approximately 85 and 100 km. The formation of a narrow emission layer during nighttime allows for the observation of this part of the atmosphere at different viewing geometries, including limb- and nadir measurements. Another advantage of the nighttime measurements is that background radiation from Earth at these wavelengths is reduced by the opacity of tropospheric and stratospheric oxygen.

In summary, the A-band oxygen emissions facilitate three different measurement modes:

- Limb sounding between 50 km and 130 km during daylight
- Nadir imaging during night time
- Tomographic measurement of a pre-selected volume during night (see below)

The tomographic measurement mode will be used to observe gravity waves. The characterization of gravity waves requires the combination of different viewing directions as in computer tomography. During nighttime, a restricted volume within the A-band layer is observed from a limb view first. When the satellite passes over the volume, it pitches to keep the volume within the

instrument's field of view. Fig 2 illustrates this observation mode. Tomographic measurements provides a benefit over existing satellite observations, because it creates truly three-dimensional data for gravity wave observation, as discussed by Preusse et al.⁸

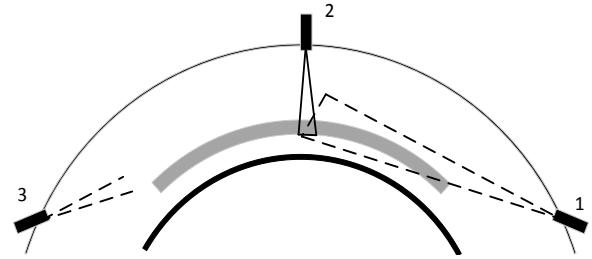


Fig 2: Illustration of the tomographic measurement concept. The dark grey area represents the middle atmosphere. The satellite is shown in limb sounding position (#1, #3) and in nadir imaging position (#2).

II.II. Temperature Retrieval

The fine structure of the A-band oxygen emission will be used for temperature retrieval, as illustrated in Fig 3. The distribution results from different rotational quantum numbers. The intensity is normalized with the highest intensity of the band. Fig 4 shows the temperature dependence of six emission lines near the center of the O_2 A-band. Lines close to the maximum show negative temperature dependence, whereas lines in the wings are positively correlated with temperature. This behavior results from the rotational (j-state) excitation of the emitting states (favoring low j-states) convoluted with their degeneracy (favoring high j-states). Thus, the atmospheric temperature can be determined by comparing two or more emission lines.

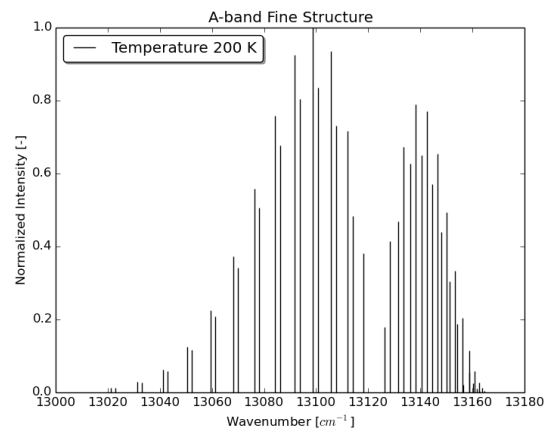


Fig 3: Fine structure of the A-band oxygen emission for a temperature of 200 K. The intensity is normalized around the maximum intensity.

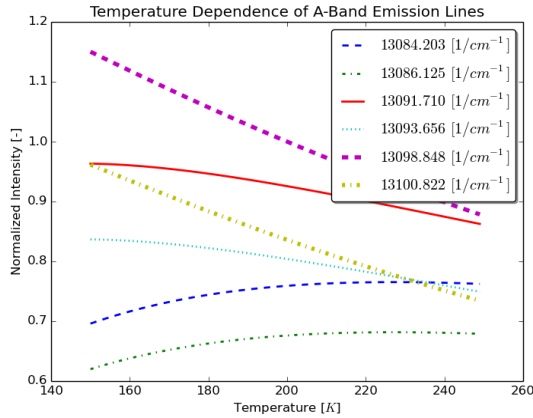


Fig 4: Temperature dependence of selected O₂ emission lines. The intensity is normalized around the maximum intensity for a temperature of 200 K.

With knowledge about the fine structure of the A-band emission and the temperature dependence of individual lines, the precision of temperature measurement can be assessed in dependence of spectral resolution and signal to noise (S/N) ratio. The spectral resolution is modelled as a convolution of normal distribution with a full-width at half-maximum (FWHM) of the spectral resolution for each emission line. The overall noise is equally divided into multiplicative and additive noise. As variables the temperature and the intensity of the A-band, expressed with a multiplicative factor for all lines, are fitted in the analysis.

Fig 5 shows the results of the analysis for a spectral resolution of 0.8 cm^{-1} and S/N ratios between 30 and 150. The standard deviation of the derived temperature to the reference temperature of 200 K is calculated with 10,000 samples.

As a result, radiance S/N ratios of 40 and 100 are needed to achieve a temperature precision of $\sim 8 \text{ K}$ in nadir and $\sim 3 \text{ K}$ in limb viewing mode, respectively.

The combination of limb and nadir measurements during tomographic measurements allows for increasing the nadir measurement precision by using limb measurements as absolute radiometric calibration. Thus, the temperature is the only fitting parameter in the retrieval algorithm, which increases the temperature measurement precision to $\sim 6 \text{ K}$ keeping the same S/N ratio of ~ 40 at nadir imaging.

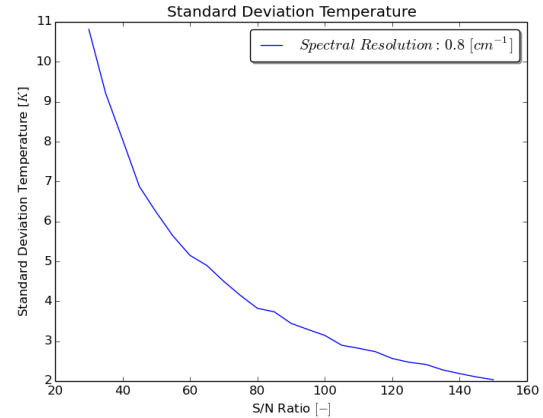


Fig 5: Precision of derived temperature in dependence of the radiance signal to noise (S/N) ratio with a spectral resolution of 0.8 1/cm . Fitting parameters are temperature and a radiometric gain. The noise is 50% multiplicative and 50% additive.

III. SPECTROMETER

To measure the intensity of individual spectral lines either a spectrometer or filters are required. At least two spectral lines need to be measured to derive the temperature from oxygen emission. A Spatial Heterodyne Spectrometer (SHS) is able to measure several spectral lines simultaneously. As an alternative, a Fabry-Perot Interferometer (FPI) in a tunable filter configuration, which scans the spectral range, is considered. In the following, both concepts are explained and compared against their expediency for this application.

III.I. Spatial Heterodyne Spectrometer (SHS)

The SHS is a relatively new instrument type, which was first implemented by Harlander et al^{9,10,11}. It can be described as a combination of a grating spectrometer and a Fourier-transform spectrometer. Its visual appearance is similar to a Michelson Interferometer (MI), where the mirrors in the arms are replaced by angled gratings. Fig 6 illustrates the concept of the SHS. Light enters the system from the left and get divided in a beam splitter (BS). Each beam diffracts at a grating (G1, G2), which is tilted with the Littrow angle. The incoming light is refracted as followed,

$$\sigma[\sin(\theta_L) + \sin(\theta_L - \gamma)] = m/d \quad (7)$$

where σ is the wavenumber of the incoming light, θ_L the Littrow angle, γ the deviation from the Littrow angle for exiting radiation, m the diffraction order and $1/d$ the grating groove density. As illustrated in Fig 6, the Littrow angle is chosen that the reflected radiation is parallel to the incoming radiation at the gratings for a specific wavenumber, the Littrow wavenumber σ_L . The two

beams are recombined at the beam splitter and constructive interference can be detected at the detector D for the Littrow wavenumber. For other wavenumbers, the refracted rays are slightly tilted with respect to the incoming radiation. This results in interference patterns after combination at the beam splitter, caused by phase differences between the two beams. Fig 6 shows the wave fronts these two beams after recombination. The phase difference is zero in the center of the detector and increases with the absolute distance x .

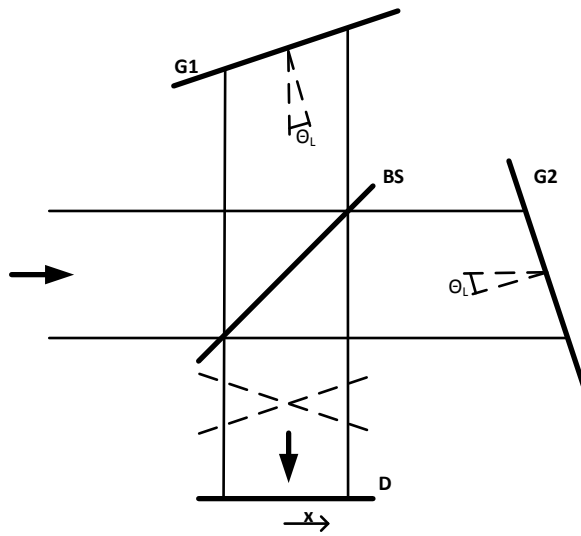


Fig 6: Schematic of the Spatial Heterodyne Spectrometer (SHS). G1 = Grating #1, G2 = Grating #2, BS = Beam splitter, D = Detector.

A strip-shaped interference pattern (in x -direction) is registered by a FPA (Focal Plane Array) located at position D (Fig 6). With an anamorphic telescope, as used for example by Englert et al.¹² the orthogonal detector dimension can be used as spatial dimension. For example, the SHS can detect the vertical distribution of the emission in limb viewing geometry.

An advantage of the SHS is that it can be built as a monolithic block, as demonstrated by Harlander et al or Doe et al.^{13,14} This reduces the size and mass of the instrument considerably, allowing, e.g., use in CubeSats. Furthermore, the accurate alignment of the instrument's components is fixated during assembly and thermal and structural gradients have only reduced influence on the alignment.

Similar to the MI, the SHS can be field-widened. But compared to the complex field-widening mechanism required for a MI, two stationary prisms between the gratings and the beam splitter allow the increase in field of view (FOV) on the order of two magnitudes by virtually rotating the image of the gratings perpendicular to the optical axis. This increases the étendue/throughput of the instrument accordingly, allowing the observation

of low emitting sources, such as the O₂ atmospheric band emissions during night.

III.II. Fabry-Perot Interferometer (FPI)

A second instrument option investigated in this paper is a FPI. This interferometer type has a considerable heritage for spacecraft systems, for example, in the TIDI instrument on the TIMED satellite or the HRDI instrument on UARS¹⁵. A FPI is also currently under development for the CubeSat Aalto-1 as a hyperspectral imager¹⁶. A FPI consists of two highly reflective plates, with a specific distance between them, where incoming light is reflected multiple times between the mirrors and only a small portion leaves the system each time. The rays interfere constructively or destructively with each other, depending on their path difference. For example for different incoming angles at a fixed wavenumber, circular interference fringes are observed by the detector with a bright area in the center. For this mission, the FPI is assumed to be used as an adjustable filter. The goal is to observe only the center of the fringe pattern, or in other words only nearly parallel rays. It is observed with a two dimensional detector, resulting in a two dimensional picture of the atmosphere. By adjusting the distance between the plates, the brightness of the image at the FPA varies depending on the wavenumber of the incoming radiation. By changing the plate distance, the band pass of the filter scans through the spectrum. Thereby, the band pass defines the spectral resolution of the measurement. Compared to the SHS, the spectrum is not measured simultaneously, but temporarily. The adjustment of the distance between the plates can be performed for example by microelectromechanical systems (MEMS) technology or piezo-actuators.

An advantage of using a FPI is the two dimensional imaging of a scene. If each spectrum requires only a short integration time, an image of approximately the same area is taken (in spite of the satellite motion during this time), showing the same state of the atmosphere. Thus, the retrieved spectrum can be used to derive the temperature.

In theory, the FPI and the SHS have the same FOV for a given specific resolving power. But field-widening the SHS increases the étendue in the order of two magnitudes compared to the FPI with equivalent aperture size. For the FPI, the aperture could be increased to match the étendue of the SHS. But the CubeSat volume and mass constraints hinder this option. Therefore, in the remaining paper, the SHS is selected as baseline concept.

IV. INSTRUMENT CONCEPT

The tomographic measurement mode with its combination of limb and nadir measurement geometries implies high demands on the field of view of the instrument. In the following analysis a circular orbit with an altitude of 600 km and an inclination of 60° is

assumed. In limb (nadir) viewing geometry, the sensor and the atmospheric volume to be observed have a distance of about 2600 (520) km. Accordingly, the field of view as well as the spatial resolution differ by a factor of approximately five for these two observations modes.

This mismatch is solved by dynamical pixel binning. In limb viewing mode a vertical field of view of 600 km imaged onto 400 detector pixels allows for a vertical resolution of about 1.5 km. For nadir imaging, the pixels are binned together by a factor of 20, because the oxygen emission intensity during nadir viewing at night is a magnitude lower than for limb measurements. The pixel binning is changed dynamically during tomographic measurement between the two extremes for limb and nadir observation.

IV.I. Optical Concept of the Instrument

In order to project a defined scene from the atmosphere onto the aperture of the SHS, an afocal telescope is needed. In addition, a lens system is required to image the resulting spectrum on the FPA.

Since the mission objectives include limb sounding during daylight, a baffle is used to reduce stray light entering the instrument. The volume requirements of the CubeSat lead to a small baffle or a deployable baffle. The concept for this mission includes an all-refractive baffle, which is translated along the long axis of the CubeSat. Its length is approximately 13 cm and it includes the aluminum rails as required in the CubeSat standard. During launch, the baffle is stowed and held with a frangibolt. When the frangibolt fires, constant force springs deploy the baffle. The internal baffle elements are parallel with the outer hull in the stowed position and rotate after deployment into their operational position, perpendicular to the hull, as in the conceptual baffle design drawing (Fig 7).

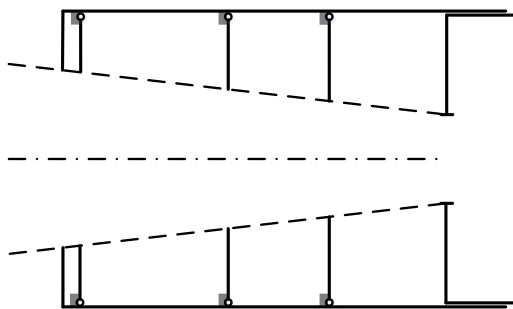


Fig 7: Conceptual baffle design

IV.II. Spectrometer Concept

The SHS is used as baseline for the spectrometer concept. As described above, the goal of temperature measurement using the oxygen A-band requires the measurement of two or more fine-structure lines. The peak intensities are around the wavenumber $13,098 \text{ cm}^{-1}$ (763.48 nm). In the

wavenumber region between $13,083 \text{ cm}^{-1}$ (764.35 nm) and $13,101 \text{ cm}^{-1}$ (763.3 nm) (spectral range 1.05 nm), there are six spectral lines, which have high intensities and also distinct temperature dependencies, see Fig 4. Other lines exist within this region, but their intensity is magnitudes lower. Each spectral line corresponds to a spatial frequency on the detector array and by adjusting the Littrow wavenumber, the distance between the spatial frequencies of the lines and the highest spatial frequency can be adjusted. The first attribute influences the distinction accuracy of each spatial frequency and thus spectral line. The second attribute directly influences the number of pixels on the detector array, because twice the highest spatial frequency should be sampled on the detector array. With these considerations, a Littrow wavenumber of $13,087.5 \text{ cm}^{-1}$ is chosen, which is equivalent to 764.09 nm . This corresponds to a spectral resolution of 0.7826 cm^{-1} , using a grating groove density of $1,000 \text{ mm}^{-1}$. The aperture size is defined in one dimension by the grating width. The other dimension is chosen to increase the étendue, while considering the CubeSat form factor. The rectangular aperture has a width and length of $7.7 \text{ mm} \times 20 \text{ mm}$. The Littrow angle is calculated to be 22.5° and the resolving power to approximately 17,000. The field of view at the gratings is increased with field widening prisms, which results in a field of view of a cone with 13.32° inner angle. This corresponds to a field widening factor of 450. A summary of design parameters is given in Table 1.

Table 1: Design parameters of the SHS

Parameter	Value
Aperture [mm x mm]	7.7 x 20
Groove Density [1/mm]	1,000
Littrow Angle [°]	22.46
Littrow Wavelength [nm]	764.088
Field of View at gratings [°]	13.32
Resolving Power [-]	16,723
Spectral Range [nm]	1.05

IV.III. Detector and Data Processing

As focal plane array (FPA) a back-illuminated Charge-Coupled Device (CCD) sensor is considered, developed specifically for scientific low intensity applications. It is characterized by a typical quantum efficiency of above 0.8 for the relevant wavelength region and a 512×512 pixel format. The operational concept requires the measurement of more than 406 horizontal slices during limb sounding to achieve a vertical resolution of 1.5 km. Therefore, individual pixels are not binned in the detector. During nadir imaging every 20 pixels are binned together in the spatial dimension. In the spectral dimension, 46 samples are taken, which corresponds to a static binning factor of 11.

The dark current of the CCD is strongly temperature dependent. Therefore the FPA is cooled down passively to a temperature of -20°C , which is feasible with a radiator panel according to a first order thermal analysis. At this temperature the CCD sensor has a dark current of 0.8 e/s , which is acceptable. With an integration time of 9 s , a S/N ratio greater than 41 can be achieved for nadir imaging during night. The long integration time has the disadvantage that the picture would smear considerably. It is countered by actively pointing the satellite on the image area during the integration. The repointing time during two images is short and can be neglected for a first order analysis.

The incoming emission radiance at the instrument during limb sounding is considerably larger and localized on 11 pixels, because of the thin emitting atmospheric layer during night time. Thus, with an integration time of 1 s , a S/N ratio of more than 100 can be achieved during night. During day, the intensity is even higher. During limb sounding, only the first 100 horizontal slices of the 406 detector rows are needed, because they image the atmosphere in the relevant altitude. For nadir imaging, the image consists of 24 pixels in the spatial dimension and 46 pixels in the spectral dimension. With 9 s integration time and continuous measurement, approximately 1.01 MB of data per orbit are collected for purely nadir imaging. Taking also a picture every 9 s during limb sounding, 4.23 MB data are generated per orbit. Tomographic measurement generates a data amount between these two values.

V. CUBESAT CONCEPT

The mission requires a three unit (3U) CubeSat form factor. The instrument occupies 1.5 units and the remaining volume is available for the bus.

An important requirement for achieving the scientific objectives is the pointing accuracy and attitude knowledge. During limb measurements, the vertical pointing knowledge shall be better than 500 m , which is equivalent to 39 arcsec . This value includes the uncertainties in the structural alignment and the pointing knowledge of the attitude determination and control subsystem (ADCS). The pointing accuracy control shall be better than 117 arcsec . Thus, the information for a specific altitude in the atmosphere can be shifted one row up or down on the FPA with the vertical resolution of 1.5 km . These requirements can be fulfilled with a high performing ADCS using a star tracker and reaction wheels as commercially available.

The communication system relies on UHF/VHF communication with the ground station for mission control and housekeeping data. Science data are transmitted with an S-band downlink. It provides high data rates of 2 Mbps during communication with the ground station. Assuming that the ground station is located in Germany, analysis indicates that the S-band

link allows the transmission of approximately 25 MB per orbit for a circular 600 km orbit with 60° inclination and with a safety factor of 2. This data volume is sufficient to satisfy the maximal 4.23 MB data volume requirement of the instrument. On-board data processing is not required, but a feasibility study will be conducted, if the data amount could be reduced on-board in such a way that it can be transmitted via UHF. The power consumption of the communication system would be decreased significantly, implying a higher duty cycle or larger margins.

The structure and the thermal system of the CubeSat are designed in a way that the alignment error is acceptable for the optical instrument and that the pointing error of the satellite is in accordance with the general pointing requirement.

Except for the radiator plate, all sides of the CubeSat are covered with solar panels for power generation. The deployable panel increases the available surface area by about 50%.

Fig 8 illustrates the 3U CubeSat with its baffle deployed. Beginning from the top, the yellow elements extending to the left and right represent dipole antennas for UHF/VHF communication. The green circle below is the S-band patch antenna. All sides except the right side in the figure have solar cells for power generation. This side is constantly looking to cold space and includes the star camera of the ADCS system and the radiator for the detector. The grey and black colored sides are placeholder for the actual coatings which are defined during detailed thermal analysis. In the figure, the baffle is depicted deployed, thus it is shifted along the long axis of the spacecraft. During launch the baffle is stowed around the instrument, so the rail ends align.

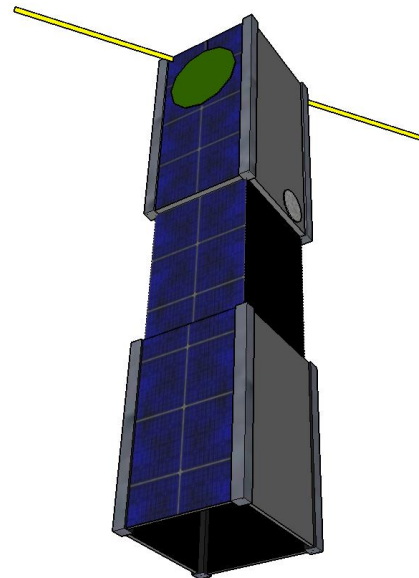


Fig 8: Illustration of the CubeSat with deployed baffle

VI. OPERATIONAL CONCEPT

This satellite is intended to work in different observational modes, depending on the different scientific objectives addressed. A standard measuring mode will be altitude resolved temperature sounding in limb viewing geometry. Coordinated measurement campaigns of ground based airglow instruments or aircraft campaigns using high resolution temperature sounders recommend to operate this satellite in tomography mode to support and complement these measurements. It is planned to allow scientific users to operate the satellite depending on their special needs for measurement modes and data requirements. A web service for the scientific community will allow to specify the to-be-measured data, by selecting the latitude and longitude region, the type of measurement, the desired S/N ratio, the spatial, spectral and time resolution and other parameters. Internal algorithms evaluate the feasibility of the measurement and afterwards the order is stacked in the task list of the satellite.

This approach can also be extended to a constellation of multiple satellites. The user interface does not change, but the internal algorithms divide the tasks between satellites and thus allow a higher performing system with increased usability for the researcher.

VII. CONCLUSION

This paper addresses a new mission concept for temperature and wave measurements in the middle atmosphere. The characterization of gravity waves will improve our understanding of the atmosphere and climate models further. The middle atmosphere temperature observations will provide data useful for understanding the dynamics and the energy budget of the atmosphere and the effects on climate change in this part of the atmosphere. This mission will also close partly the observational gaps to be expected during the next years in middle atmosphere sounding.

The satellite concept is based on the popular CubeSat standard. The focus on small satellites allows for highly flexible observation geometries and innovative modes of operation. A tomographic measurement mode will allow

for the measurement of temperature at unprecedented spatial scales for the analysis of wave patterns in the atmosphere. The Spatial Heterodyne Spectrometer (SHS) seems very suitable to meet the scientific specifications of the mission. It can be designed in a way that it is able to measure six spectral lines of the A-band oxygen band with distinct temperature dependence of the intensities. The analysis suggests that the temperature can be retrieved better than 3 K precision with a vertical resolution of 1.5 km for limb sounding (day and night) and 8 K precision at nadir imaging. The tomographic measurement has increased accuracy at nadir with 6 K.

Especially during limb sounding in daylight, background radiation is of major concern. It is reduced with a deployable baffle, which extends along the long axis of the satellite.

The satellite bus includes a high performing attitude control system with reaction wheels and a star camera, which is required for limb sounding. The communication relies on a UHF/VHF link for housekeeping data and an S-band link for science data. The operational concept envisions a distributed user environment in which users submit their mission requests and receive data directly to and from the satellite system with minimal interaction of the satellite operator.

This mission concept is intended to act as a pathfinder for a future remote sensing constellation. The constellation objectives are to observe the Earth's middle atmosphere and to close the existing measurement gaps. The constellation satellites are all based on the CubeSat form factor with a standardized bus. The instruments will use same technologies, but with configurations for different atmospheric bands and operational modes. Thereby, a goal is to keep each satellite instrument function limited to decrease costs/ manufacturing time and increase the reliability of each satellite. Together as a constellation, the satellites will be capable of providing valuable scientific data similar to large scientific satellites.

VIII. REFERENCES

¹ Intergovernmental Panel on Climate Change (2014): Climate Change 2013: The Physical Science Basis. Working Group I Contribution to the IPCC Fifth Assessment Report. Cambridge: Cambridge University Press.

² Baldwin, Mark P.; Dunkerton, Timothy J. (1999): Propagation of the Arctic Oscillation from the stratosphere to the troposphere. In *J. Geophys. Res.* 104 (D24), pp. 30937–30946.

³ Gray, L. J.; Beer, J.; Geller, M.; Haigh, J. D.; Lockwood, M.; Matthes, K. et al. (2010): Solar Influences on Climate. In *Rev. Geophys.* 48 (4), pp. RG4001. DOI: 10.1029/2009RG000282.

⁴ Garcia, et al., Simulations of secular trends in the middle atmosphere, *J. Geophys. Res.*, 112, doi: 10.1029/2006JD008485, 2007.

⁵ Marsh, D., et al., Modeling the whole atmosphere response to solar cycle changes in radiative and geomagnetic forcing, *J. Geophys. Res.*, 112, doi: 10.1029/2006JD008306, 2007.

⁶ Smith, A. (2012): Global Dynamics of the MLT. In *Surv Geophys* 33 (6), pp. 1177-1230. DOI: 10.1007/s10712-012-9196-9.

⁷ Bucholtz, A.; Skinner, W. R.; Abreu, V. J.; Hays, P. B. (1986): The dayglow of the O₂ atmospheric band system. In *Planetary and Space Science* 34 (11), pp. 1031–1035. DOI: 10.1016/0032-0633(86)90013-9.

⁸ Preusse, P.; Schroeder, S.; Hoffmann, L.; Ern, M.; Friedl-Vallon, F.; Ungermann, J. et al. (2009): New perspectives on gravity wave remote sensing by spaceborne infrared limb imaging. In *Atmospheric Measurement Techniques* 2 (1), pp. 299–311.

⁹ Harlander, John M.; Roesler, Fred L. (Eds.) (1990): *Spatial heterodyne spectroscopy: a novel interferometric technique for ground-based and space astronomy* (1235). Available online at <http://dx.doi.org/10.1117/12.19125>.

¹⁰ Harlander, John M.; Roesler, Fred L.; Cardon, Joel G.; Englert, Christoph R.; Conway, Robert R. (2002): Shimmer: A Spatial Heterodyne Spectrometer for Remote Sensing of Earth 's Middle Atmosphere. In *Appl. Opt.* 41 (7), p. 1343. DOI: 10.1364/AO.41.001343.

¹¹ Harlander, J.; Reynolds, R. J.; Roesler, F. L. (1992): Spatial heterodyne spectroscopy for the exploration of diffuse interstellar emission lines at far-ultraviolet wavelengths. In *ApJ* 396, p. 730. DOI: 10.1086/171756.

¹² Englert, Christoph R.; Harlander, John M.; Owrutsky, Jeffrey C.; Bays, J. T. (2005): SHIM-Free Breadboard Instrument Design, Integration, and First Measurements. DTIC Document.

¹³ Harlander, John M.; Roesler, Fred L.; Englert, Christoph R.; Cardon, Joel G.; Conway, Robert R.; Brown, Charles M.; Wimperis, Jeff (2003): Robust Monolithic Ultraviolet Interferometer for the SHIMMER Instrument on STPSat-1. In *Appl. Opt.* 42 (15), p. 2829. DOI: 10.1364/AO.42.002829.

¹⁴ Doe, Richard A.; Watchorn, Steven; Butler, James J.; Xiong, Xiaoxiong; Gu, Xingfa (2011): Climate-monitoring CubeSat mission CM2: a project for global mesopause temperature sensing. In: *SPIE Optical Engineering + Applications*. San Diego, California, Sunday 21 August 2011: SPIE (SPIE Proceedings), pp. 81530Q.

¹⁵ Shepherd, G. G. (2002): *Spectral imaging of the atmosphere*. San Diego, Calif: Academic Press (International geophysics series, v. 82).

¹⁶ Kestilä, A.; Tikka, T.; Peitso, P.; Rantanen, J.; Näsilä, A.; Nordling, K. et al. (2013): Aalto-1 nanosatellite – technical description and mission objectives. In *Geosci. Instrum. Method. Data Syst.* 2 (1), pp. 121–130. DOI: 10.5194/gi-2-121-2013.